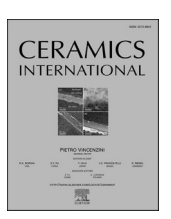
ELSEVIER

Contents lists available at ScienceDirect

Ceramics International

journal homepage: www.elsevier.com/locate/ceramint





The effects of in-situ synthesized TiC on the performance improvement of nickel-based composite coatings for rail repair

Juncai Li ^{a,b}, Yue Yang ^{a,b}, Liaoyuan Chen ^c, Bojun Sun ^{a,b}, Zixuan Wang ^{a,b,*}, Tianbiao Yu ^{a,b,**}, Ji Zhao ^{a,b}

- ^a School of Mechanical Engineering and Automation, Northeastern University, Shenyang, 110819, People's Republic of China
- b Liaoning Provincial Key Laboratory of High-end Equipment Intelligent Design and Manufacturing Technology, Shenyang, 110819, People's Republic of China
- ^c School of Mechatronics Engineering, Henan University of Science and Technology, Luoyang, 471000, People's Republic of China

ARTICLE INFO

Handling Editor: Dr P. Vincenzini

Keywords: TiC/Ni In-situ synthesis Physical phase Microstructure Microhardness Wear resistance

ABSTRACT

With the increase in train speed and axle weight, the quality and service life of the rail (U71Mn steel) are more demanding. Aiming at the excellent properties of nickel/nickel-based alloys and ceramic materials, this paper prepares TiC/Ni45 composite coatings for rail repair by in-situ synthesis of ceramic phases using laser cladding technology. The effects of in-situ synthesized TiC on the physical phase, microstructure, microhardness and wear resistance were investigated and discussed in detail. The results show that the reaction of in-situ synthesized TiC can proceed positively, and the microstructure of the cladding layer mainly consists of the segregation of Cr, TiC particles, and substrate phase. With the increase of nickel-coated graphite and titanium powder, the average microhardness value of the cladding layer increased, and the average friction coefficient and wear volume decreased. When the mass fraction of (Ti + C) reaches 15 wt%, the average friction coefficient of the cladding layer reaches the minimum value. When the mass fraction reaches 20 wt%, the average microhardness of the cladding layer reaches 2.65 times that of the substrate, and the wear mechanism is transformed from mainly adhesive wear to abrasive, oxidative, and fatigue wear.

1. Introduction

With the increase in train speed and axle weight, the rail loading environment becomes more complex and harsh, and the working conditions of the wheel-rail friction are more and more severe [1–4]. Therefore, as a most widely used rail material, requirements for the quality and service life of U71Mn steel are increasing. Nickel (Ni) or Ni-based alloys with excellent high-temperature stability, corrosion resistance, and plasticity, are widely used in aerospace, automotive, communications, electronics, etc [5–7]. The ceramic materials due to their high hardness, good wear resistance, and thermal stability, have proved to be the ideal reinforcement for Ni-based composite coatings [8, 9].

At present, the metal additive manufacturing technology can be divided into wire arc additive manufacturing (WAAM), electron beam additive manufacturing (EBAM) and laser additive manufacturing (LAM) according to the heat source. Laser cladding technology has

several significant advantages, including high energy density, low heat input, high efficiency and precision, fast response and excellent forming results. This technology is mainly applied to repair parts with high precision and strict performance standards [10,11]. Using laser cladding technology, the excellent properties of metal materials such as high strength and high toughness can be combined with the excellent wear and corrosion resistance of ceramic materials, which can further enhance the surface properties of materials. However, due to the large difference in thermophysical parameters between the directly externally added ceramic phase and the matrix material, the compatibility is poor, which decreases the interfacial bonding [12,13]. It can easily become a source of cracks. In contrast, the ceramic phase generated by in-situ synthesis generally solidifies and crystallizes from the liquid phase or nucleates, and grows up as a solid-state phase transition [14]. The thermodynamic properties are relatively stable. the generated particles are uniformly distributed and have good wettability to the matrix.

In recent years, researchers have conducted a lot of research on the

^{*} Corresponding author. School of Mechanical Engineering and Automation, Northeastern University, Shenyang, 110819, People's Republic of China.

^{**} Corresponding author. School of Mechanical Engineering and Automation, Northeastern University, Shenyang, 110819, People's Republic of China. E-mail addresses: wangzx@mail.neu.edu.cn (Z. Wang), tbyu@mail.neu.edu.cn (T. Yu).

application of laser cladding technology on rail steel and found that the generation of a cladding layer on the rail steel surface can effectively improve wear resistance [15]. Clare et al. [16]fused-coated high-hardness work-hardening alloys, including Ni-based alloys, cobalt-based, and martensitic high-strength alloys on the rail substrate for repairing and strengthening rails. The results show that the laser cladding process after parameter optimization can obtain the cladding layer with high hardness, no cracks, and no porosity. Lewis et al. [17] explored the effect of different materials of the cladding layer on the wear and contact fatigue performance of the rail through the two-wheel grinding test. The results showed that the use of Stellite1 reduced the wear by at least 70 % and increased the contact fatigue damage initiation life. Guo et al. [18]studied the properties of the Co-based fused cladding layer on wheel rails and found that the fused cladding layer mainly exists in the form of dendritic and eutectic organization. The combination of the fused cladding layer and the matrix is coarse columnar crystals and the hardness of wheel rails was greatly improved. Qi et al. [19] used laser cladding technology to repair seamless rails. The repair of Fe-based alloy powder with vanadium constitutes a uniform organization in the cladding area without defects, and wear resistance is improved, results showed the presence of less martensite in the fusion cladding layer. Yang et al. [20] used Fe-based alloy powder to strengthen the surface of U71Mn rails by coaxial powder feeding method. The observation using the penetration flaw detection method found that in large-area laser cladding, cracks were related to the thickness of the cladding layer. When the thickness of the cladding layer is around 1 mm, a crack-free cladding layer can be obtained. The results of static load compression tests indicate that the cladding can withstand static loads without cracking.

The above studies have shown that the repair of rails can be realized by laser cladding, but it has also been found that the hardness and wear resistance of the repaired rails are difficult to meet the requirements by using a single alloy powder. Therefore, the addition of ceramics to improve the wear resistance of a single alloy, and then achieve the repair of key components has become a research hotspot. Jiang et al. [21] conducted laser cladding experiments on 45 steel surfaces. Ni-based alloy powder was used and WC was added as the reinforcing phase to prepare a single-pass laser cladding gradient coating. The results showed that the microhardness of the top of the cladding layer could reach 70 HRC, which is 3-4 times higher than that of the substrate. Li et al. [22] clad WC/Ni60A composite powders with WC on the surface of H13 steel. By observing the microstructure of the cladding layer, it was found that the size of carbide particles increased with the increase of WC mass fraction, and the hardness of the cladding layer was increased up to 4 times. Cao et al. [23] prepared ceramic coatings by cladding Ni60/TiC hybrid powders on the surface of 45 steel. The hardness, friction and wear properties, and corrosion resistance of the coatings with different TiC contents were examined. The results showed that the addition of TiC could improve the wear and corrosion resistance of the coatings, as well as the hardness of the coatings. The best wear and corrosion resistance of the coating was obtained when the TiC content in the composite powder was 20%-30 %.

Cui et al. [24] enhanced the wear and corrosion resistance of Ni-based coatings by in-situ synthesizing ${\rm TiC-TiB_2}$ ceramics with TAO, B₄C, and Ni-coated graphite via laser cladding. Coatings with 3 wt% B₄C and 8 wt% Ni-coated graphite exhibited the lowest wear volume (26.47% reduction) and improved corrosion resistance. The optimal performance was attributed to the increased size of the ceramic phase, which changed the wear mechanism and raised the coating impedance. This research offered insights into developing high-performance Ni-based coatings. Hu et al. [25] studied the wear resistance enhancement of tunnel boring machine disc cutter rings. Ni₃Ta-TaC reinforced Ni-based coatings are synthesized on 5Cr5MoSiV steel by laser cladding with Ni, Ta, and Ni-coated graphite powders, with TiC added to inhibit cracking. The coatings exhibited in-situ formation of Ni3Ta and TaC, with small TaC particles aggregating around TiC. The addition of TiC effectively

inhibited lath-shaped Ni_3Ta formation and cracks, resulting in 4 times higher wear resistance than the substrate. This research provided insights into improving the wear resistance of tunnel boring machine components. Li et al. [26] investigated Ni62 composite coatings on 65Mn steel prepared by laser cladding with WC and TiC particles. Cracks penetrated the coating and occurred at the interface with the substrate. Adding CeO_2 refined the structure and reduced defects. The wear of the coating was mainly caused by the alternating effects of adhesive, delamination, and abrasive wear.

The microhardness and wear resistance of the alloy are effectively improved by the direct addition of ceramics. However, it was also found that defects such as cracks and porosity resulted in poor bonding quality due to the difference in thermophysical parameters between the matrix and the ceramic. The in-situ synthesis of ceramics to improve the wear resistance of the material provides a perfect solution to these problems. Therefore, Ni-based alloy powder, titanium powder, and Ni-coated graphite powder were selected as the deposition materials. The in situ synthesized TiC/Ni45 composite coating was prepared by laser cladding to improve the microhardness and wear resistance of laser-repaired areas of U71Mn steel. Besides, the effects of different contents of (Ti + C) on the physical phase composition and microstructure of the composite coatings were also investigated by X-ray diffractometer, scanning electron microscope, and energy spectrometer. The microhardness, and wear resistance of the composite coatings were examined by a microhardness tester and multifunctional material surface property tester, and the wear mechanism was also analyzed. The results of this study are aimed at improving the remanufacturing performance of waste rails, extending service life, and promoting sustainable development.

2. Experiments

2.1. Material and experimental method

The equipment used in this study is a coaxial powder-feed laser cladding system, which mainly consists of a laser, powder feeder, chiller, KUKA robot, laser cladding head, etc. The maximum power and wavelength of the CW fiber laser source are 500 W and 1070 nm. The substrate used is U71Mn rail steel, and the chemical composition can be seen in Table 1. The chemical composition of Ni45 powder can be seen in Table 2. A section of standard specification rail steel was taken and truncated, as shown in Fig. 1 (a). Through the wire-cutting method, the substrate was prepared with a length, width, and height of $100 \times 70 \times 10 \text{ mm}^3$. Before the laser cladding experiment, the surface of the substrate was sanded, cleaned, and dried to prevent impurities and rust on the surface from affecting the cladding experiments.

In the experiment, Ni45 alloy powder is selected as the initial phase, which is composed of γ -Ni, Cr_3C_7 , and CrB phases, as shown in Fig. 1 (b) and (c). Meanwhile, to improve the performance of the laser cladding layer, titanium powder, and Ni-coated graphite powder are added to the initial powder to in-situ synthesize the reinforcing phase of titanium carbide. Considering the low density of pure graphite powder, it is not uniformly mixed with other powders, which is easy to be deposited on the upper surface of the composite powder and difficult to enter into the molten pool. Therefore, the nickel-coated graphite powder was chosen instead, in which the nickel-to-graphite mass ratio was 3:1. Five different mass fractions of (Ti + C)/Ni45 composite powders were prepared according to the different contents of Ti + C. The atomic ratio of Ti and C in each sample was 1:1. The powders were first mixed thoroughly with a planetary ball mill for 2 h to ensure their homogeneity before the

Table 1The chemical composition of U71Mn steel.

Elements	С	Si	Mn	P	S	Fe
Content	0.65~	0.15~	1.10~	≤0.030	≤0.030	Bal.
	0.76	0.35	1.40			

Table 2The chemical composition of Ni45 powder.

Elements	С	Cr	Fe	Si	В	Mn	Ni
Content	0.45	12.0	10.0	4.0	2.4	0.1	Bal.

experiment, and then dried in a dryer at 120 $^{\circ}$ C for 2 h to ensure their fluidity. The ball to powder weight ratio for dry ball-milling operation is around 4:1. The powder content distribution for each workpiece and laser cladding process parameters is listed in Table 3. The powder delivery gas and the protective gas were argon with 99.99 % purity, and the flow rates were 8.0 L/h and 12 L/h. In addition, the surface of the substrate was polished with sandpaper, until the polished surface was mirror-like. Then the surface was cleaned with alcohol to remove the dirt before the experiment.

2.2. Characterization

Fig. 2 shows the experimental sample preparation process. After the laser cladding process, the workpiece was divided into two parts by wire cutting along the vertical of the scanning direction. One part was used for XRD and wear resistance experiments, and the other part was used for microstructure and microhardness measurements. The metallographic workpieces were prepared in the following steps in order: the surfaces of the workpieces were polished by SiC sandpapers with different grain sizes to 2000 mesh, and then polished with diamond polishing paste of 2 μm size on a polishing machine. The surface line roughness of polished workpieces is as low as around 80 nm. The surface of the workpiece was etched with aqua regia. Before all the tests, the samples were ultrasonically cleaned in alcohol for 2 min, and the workpieces were dried with an air blower.

The phase compositions were analyzed by X-ray diffractometer (XRD, X Pertpro, The Netherlands, Cu - K α radiation). The microstructure of the cladding coating was examined by scanning electron microscopy equipped with energy dispersive spectroscopy (SEM and EDS, ZEISS Ultra Plus). The microhardness at the cross-section was measured using a Vickers indentation tester (HV-1000, Shanghai) with a load of 500 g and a holding time of 12s at an interval of 300 μm . Nine measurement points from the surface of the substrate to the surface of the cladding layer, making a total of 13 points. A multifunctional material surface property tester (MFT-4000, Lanzhou Huahui Instrument Technology Co., Ltd.) was used to carry out the scratch and wear tests for a comprehensive evaluation of its wear performance. Reciprocating friction tests were carried out at room temperature using Al₂O₃ balls with a diameter of 5 mm (hardness >90HRC). The specific parameters are a normal load of 15 N, a unidirectional stroke length of 5.0 mm, a speed of 200 mm/min, and a time of 30 min. The 2D and 3D wear

surfaces were obtained by laser confocal microscopy (OLS4000, Japan).

3. Results and analysis

3.1. Macro morphology

The experimental results are shown in Fig. 3. It can be seen that the surface of the pure Ni45 cladding layer has a certain degree of luster. With the addition of (Ti + C), the surface of the cladding layer is gradually getting black. The surface quality of the cladding layer is deteriorated, and all have varying degrees of cracking. When the mass fraction of (Ti + C) reaches 20 %, the cracks increase and gradually expand. And more pores appear, which seriously affects the performance of the coating. Compared with the other samples, the surface of sample S3 has relatively fewer defects.

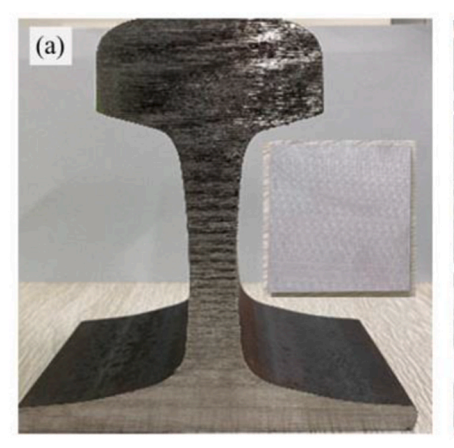
With the increase in the mass fraction of composite powder (Ti + C), there are more and more hard phases in the cladding layer. It will increase the brittleness of the cladding layer while increasing the hardness of the whole cladding layer, and cracks are easy to generate [27,28]. Furthermore, due to the temperature difference between the cladding layer temperature and room temperature, the differences in thermal expansion coefficients between the hard particles and the matrix result in different cooling shrinkage rates of the cladding layer [29,30]. It makes the cladding layer extruded by the formation of thermal stresses. When the strain caused by the thermal stresses is greater than the limit of the material, cracks will be generated.

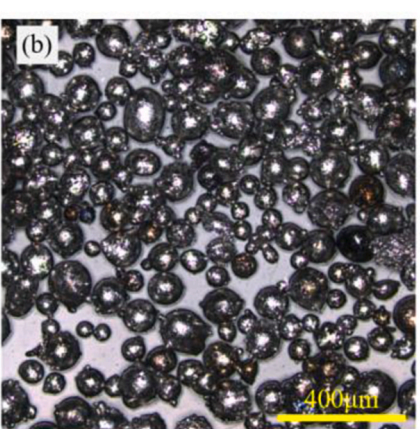
3.2. Analysis of the physical phase of the cladding layer

The XRD patterns of five nickel-based composite coatings with different Ti + C contents can be seen in Fig. 4. By comparing the PDF card analyses, the main phase of all workpieces is Ni. In workpiece S0 without Ti and C, the $Fe_3Mn_2Si_3$ phase and trace amounts of the MnB phase appeared. The high temperature during the laser cladding process

Table 3The ratio of the mass fraction of each sample and the process parameters.

Sample	Component content			Process parameters			
	Ni45	Ti	Ni- coated C	Laser powers	Scan speed	Powder feeding rate	Overlap rate
S0	50	0	0	431 W	5.38	1.03r/min	34.5 %
S1	46	2	2		mm/s		
S2	42	4	4				
S3	38	6	6				
S4	34	8	8				





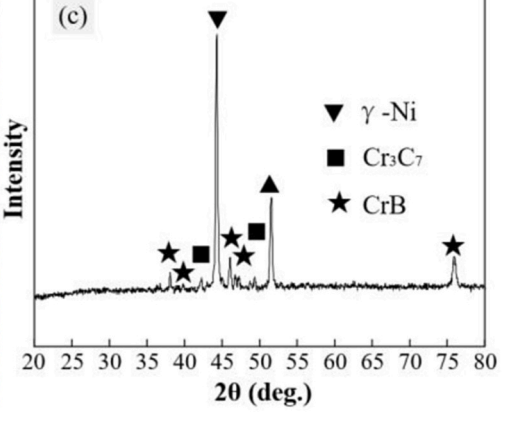


Fig. 1. Experimental materials: (a) rail sample; (b) Optical image of Ni45 powder; (c) XRD results of Ni45 powder.

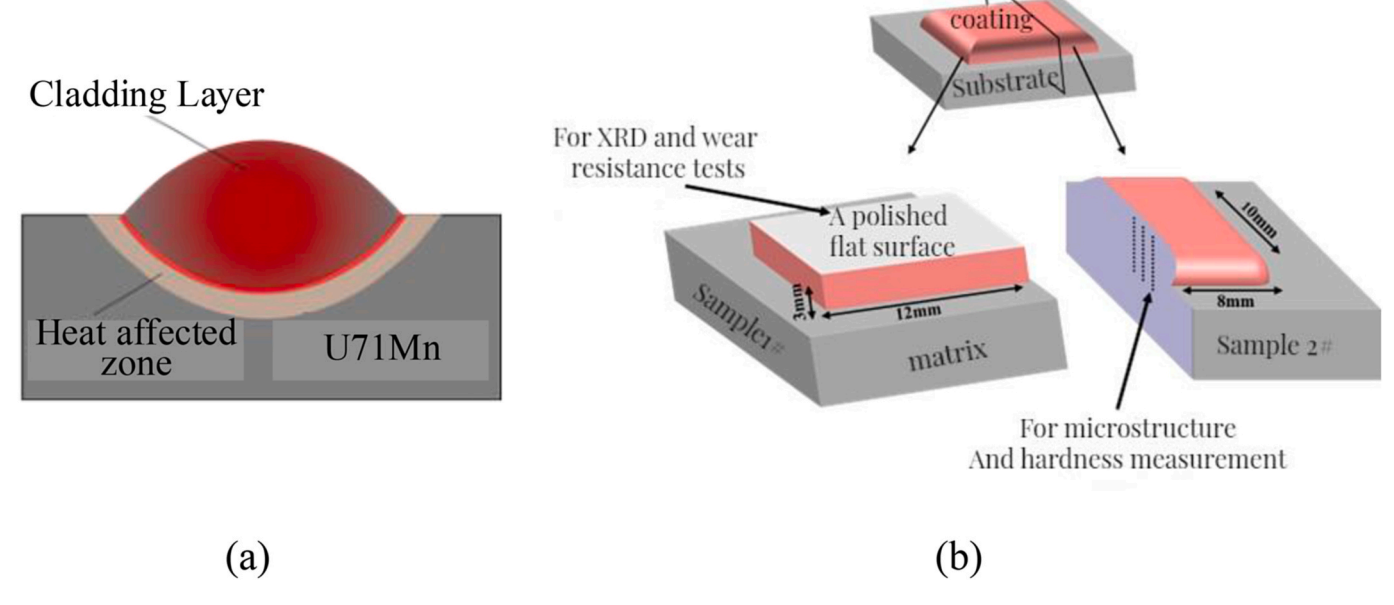


Fig. 2. The schematic diagram: (a) the cross-section of single track cladding; (b) the experimental samples preparation process.

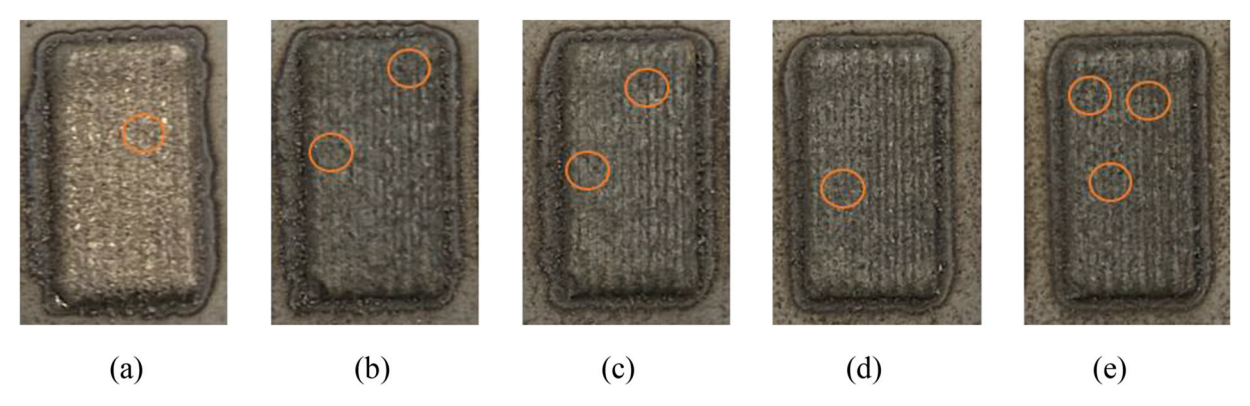


Fig. 3. Optical images of composite coating surfaces: (a) S0: Ni45; (b) S1: Ni45 + 5 % (Ti + C); (c) S2: Ni45 + 10 % (Ti + C); (d) S3: Ni45 + 15 % (Ti + C); (e) S4: Ni45 + 20 % (Ti + C).

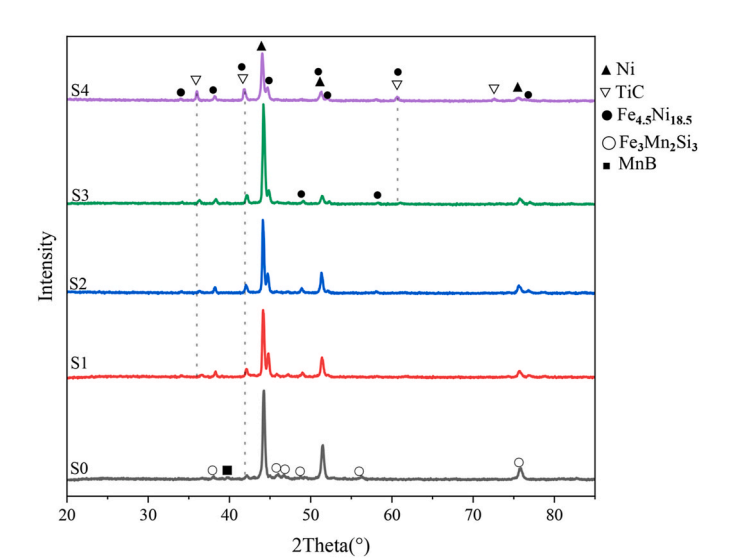
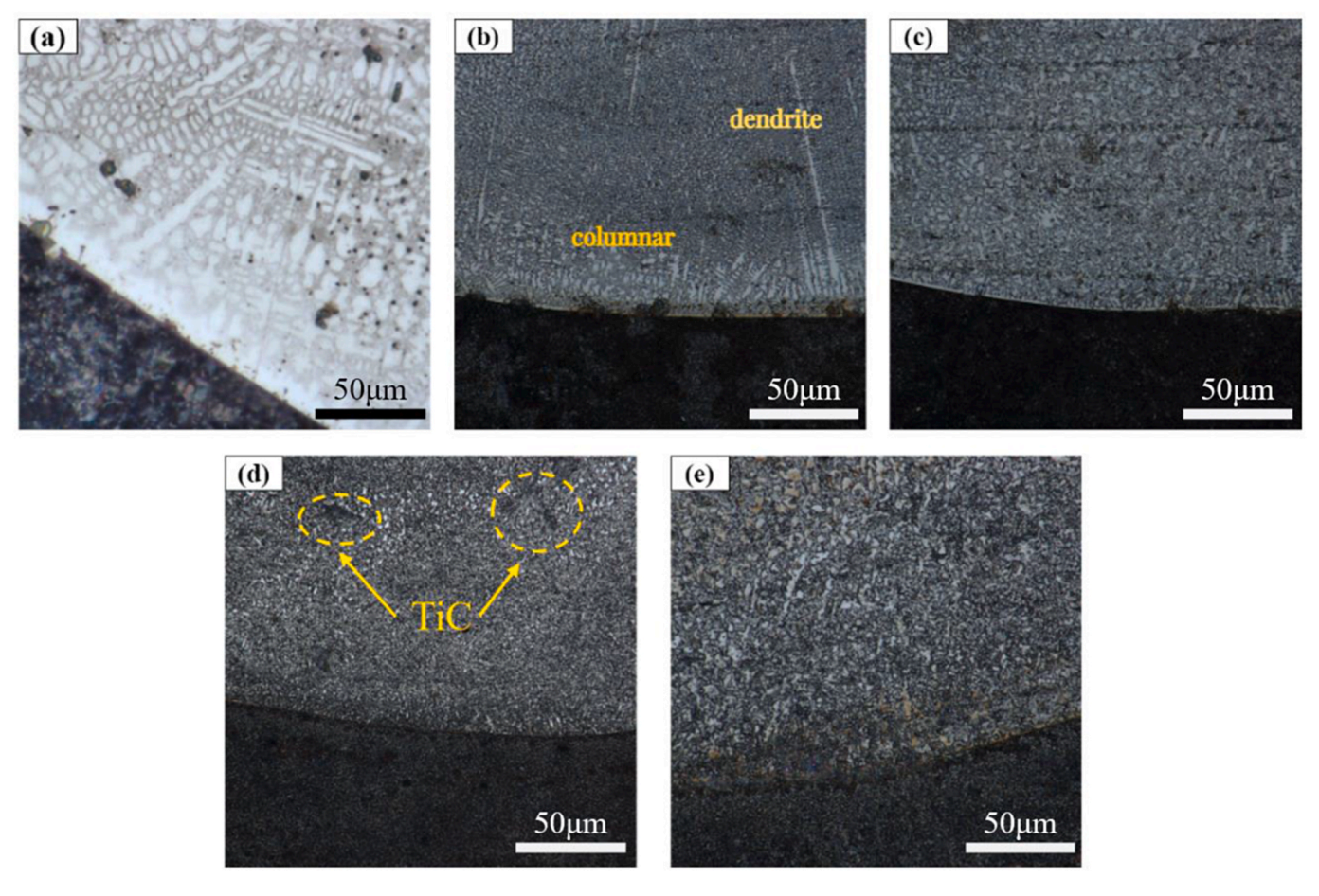


Fig. 4. The XRD analysis results of composites with the different mass fraction.

caused to generation of Fe₃Mn₂Si₃ and MnB phases. Workpiece S1 has Fe-based solid solutions such as Fe_{4.5}Ni_{18.5} and Fe₃Mn₂Si₃ in addition to the Ni main phase. With further increase in the mass fraction of C and Ti, Fe₃Mn₂Si₃ in workpiece S3 disappeared and a trace of TiC phase appeared with three strong peaks at 41.8°, 35.9° and 60.5°. The new phases did not appear in S3 and S4 as the C and Ti contents increased. However, it is noteworthy that the increase in C and Ti content leads to a significant enhancement of the TiC peaks, especially in S4. However, no Cr₃C₂ and Cr₇C₃ phases were found in the workpieces, which may be due to the low content of Cr in the melt pool, or the Carbides of Cr reacting with the free Ti in the melt pool to generate a more stable TiC phase, which is similar to the results of the study [5,31]. Overall, the appearance of TiC peaks proves that the TiC phase can be directly in-situ synthesized by Ti powder and nickel-coated graphite powder during the laser cladding process, but it is necessary to reasonably control the amount, proportion, and the way of addition of Ti and C, to facilitate the generation of diffusely distributed TiC phases.

3.3. Microstructure analysis

As shown in Fig. 5, it shows the microstructures of the initial Ni45 cladding layer and the in situ generation of nickel-based composite coatings with different contents of TiC. As shown in Fig. 5 (a), A large



 $\textbf{Fig. 5.} \ \ \textbf{The microstructure in the bottom zone of the cladding layer (a) S0; (b) S1; (c) S2; (d) S3; (e) S4. \\$

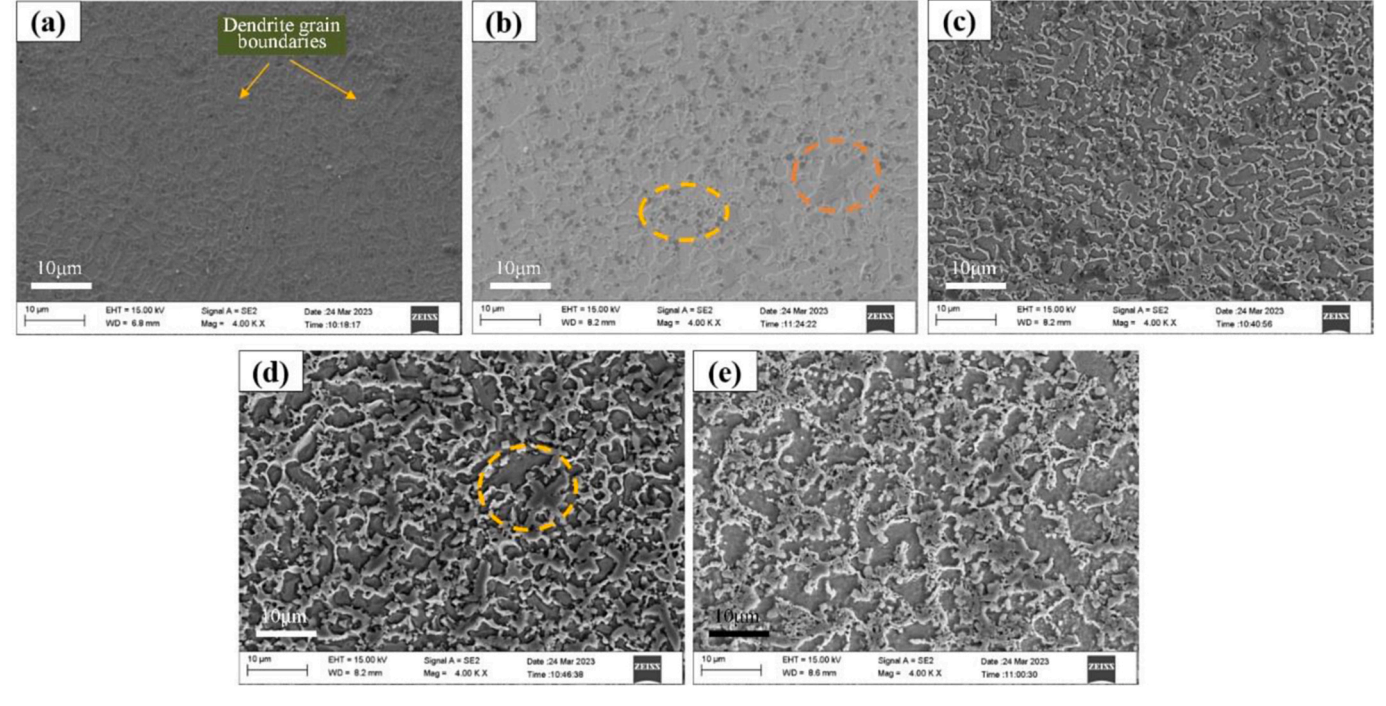


Fig. 6. The microstructure in the middle zone of the cladding layer (a) S0; (b) S1; (c) S2; (d) S3; (e) S4.

number of coarse columnar crystals and cellular crystals with obvious orientation were formed at the bottom of the cladding layer. At higher temperature gradients and low cooling rates, the bottom microstructure of the cladding layer preferentially grew in the form of planar crystals [32]. However, these crystals transformed into columnar crystals and grew along the direction of the temperature gradient when they were subjected to perturbation and other growth barriers. From Fig. 5 (b)-(e), it can be seen that the microstructure of the cladding layer changed after the addition of Ti powder and Ni-coated graphite. The microstructure gradually became fine and dense. This is because the TiC phase in-situ synthesis provides a large number of nucleation sites, which in turn promotes the nucleation process of the grains and the formation of more new grains. Besides, the in situ synthesized ceramic particles weakened the heat flow density at the bottom of the melt pool and inhibited the formation of columnar grains [27,33]. This effectively improved the bond strength of the in situ TiC-reinforced composite coating to the substrate and decreased the spalling in the repaired area.

As shown in Fig. 6, it shows the microstructure of the middle part of each cladding layer. From Fig. 6 (a), it can be seen that when (Ti+C) is not added, the cladding layer has a clear interface, fewer impurities, and obvious dendrite boundaries, which is mainly due to the temperature gradient generated by the rapid cooling and heating during the cladding process as well as the uneven temperature distribution. As shown in Fig. 6 (b), when 5 % (Ti+C) was added, the black second phases of different shapes began to precipitate at the dendrite boundaries as well as at the surface of the dendrites, and the microstructure consists of lamellar white precipitated phases, black precipitated phases, and grey matrix.

To determine the composition of the precipitated phase, the EDS spectrometer was used to carry out a surface scan of the region, and the results are shown in Fig. 7. It shows that a large number of Ni, Ti, Cr, and C elements and a small amount of Si, Fe can be observed. The Ti element overlaps with the C element very much, and the Cr element segregation, so it is inferred that the region is mainly the γ -substrate phase and TiC according to XRD results.

With the increased mass fraction of (Ti+C), more and more phases are precipitated and more uniformly distributed. Fig. 8 shows the results of the scanning energy spectrum analysis of the S4 cladding layer. Combined with the surface scanning results of the workpiece S1, the content of the Fe element in S4 is slightly higher than that of the other elements in addition to the elements Ni and C. As the Fe element is the main component in the composition of the substrate, the alloying elements in the substrate diffuse to the cladding layer during the cladding process, which can also maintain a certain dilution rate. And then ensure the bonding strength of the cladding layer with the substrate, so the content of Fe element in the cladding layer increases.

To further confirm the physical phase composition of the cladding layer, EDS point scan analysis was performed on typical areas of the cladding layer on workpiece S3 with 15 wt% (Ti + C), as shown in Fig. 9. The precipitation phases at Point 1 and Point 4 are petaloid, and the EDS point scanning results are shown in Fig. 10 (a) and (d). It shows that the two points are enriched with Ti and C elements, with the mass fractions accounting for more than 90 %. It can be seen that the particles at these two places are mainly composed of Ti and C, and the atomic mass ratio is close to 1:1, which confirms the existence of the in-situ synthesized TiC [12,34]. At the same time, the surface of TiC particles and the substrate have no other attachments. This can also ensure the bonding strength of TiC particles to the substrate, which ensures that the coating will not fail due to interfacial rupture [35,36].

Point 2 is the matrix phase. The EDS point scanning results are shown in Fig. 10 (b), which is dominated by Ni elements, followed by Fe elements, and a small amount of Cr elements. It can be judged that the substrate phase is a γ -Ni-based solid solution, which is also consistent with the conclusions drawn from the previous XRD analysis.

Point 3 shows a square shape. Through the EDS point scanning results, it can be seen that the point is dominated by the elements Ti and C, as well as a small amount of Cr elements. Therefore the main component at this site is TiC particles. Due to the complexity and variability of the laser cladding process, under the interplay of the grain's properties and other phases, a relatively ideal growth environment may occur. It puts the TiC crystals in an equilibrium state, and under these relatively ideal conditions, the particles within the cladding layer will be presented in a square shape.

A surface scan in the top zone of sample S4 cladding layer was performed and the results are shown in Fig. 11. It can be seen that the whole microstructure is uniformly distributed, in which the Ti and C elements overlap extremely well. The TiC precipitation particles have different shapes, including clusters, squares, and petals. This is because in the cladding process, a large amount of heat inside the melt pool causes TiC particles to melt locally, and these particles impact each other during movement and sinter to form new particles [37,38]. Petal-shaped TiC is mainly formed by aggregating locally melted TiC particles around a core of granular TiC precipitated from in-situ synthesis. Cluster-shaped TiC is formed by the reaction between supersaturated Ti and C atoms in the liquid melt pool and the rapid decrease in the melt pool temperature.

Based on the above phenomenon, the process of in-situ synthesis of TiC particles by laser cladding was analyzed. The composite powder arrives at the upper surface of the substrate under the drive of the powder-feed gas. It absorbs a large amount of heat and melts, then melts with the surface layer of the substrate to form a melt pool. Since the melting point of graphite in the nickel-coated graphite is high, when the nickel-coated layer on the periphery of the graphite in the melting bath

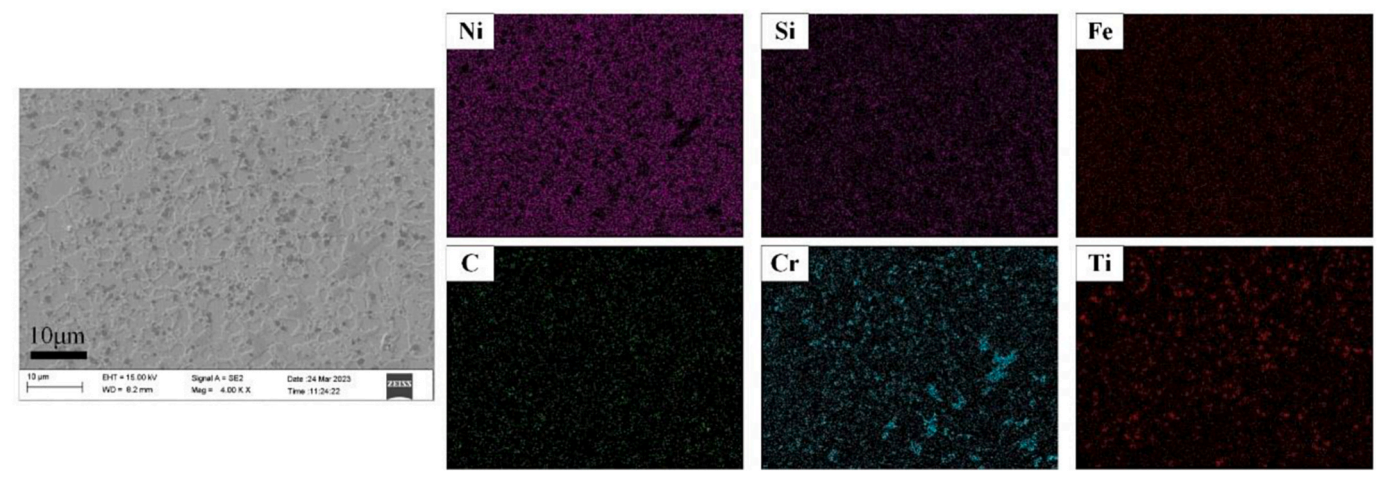


Fig. 7. The EDS surface scan results of sample S1.

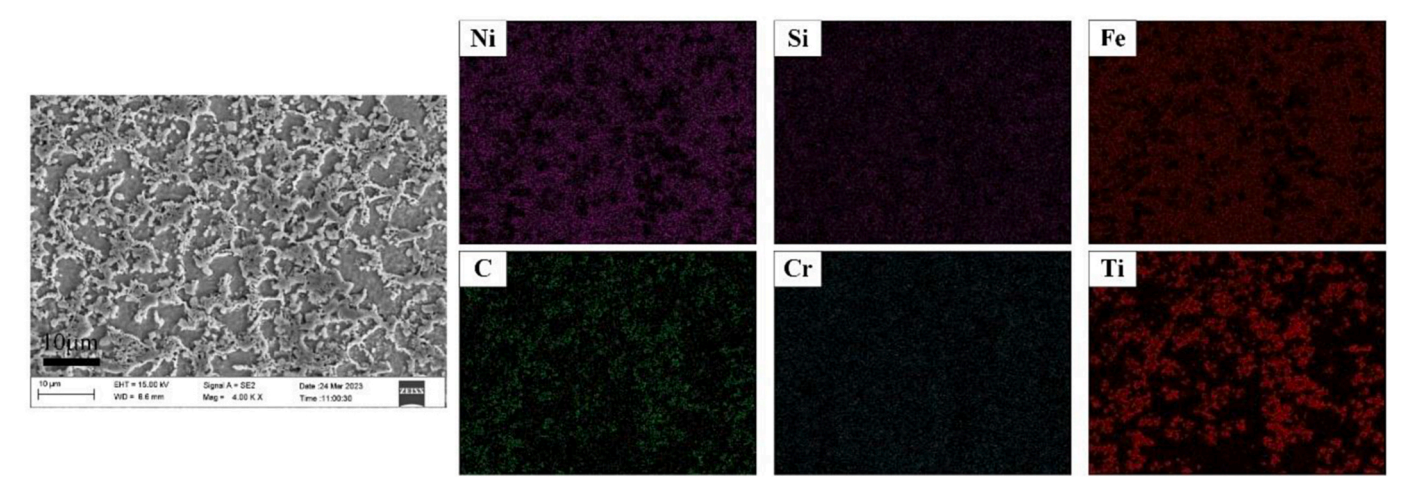


Fig. 8. The EDS surface scan results in the middle zone of sample S4.

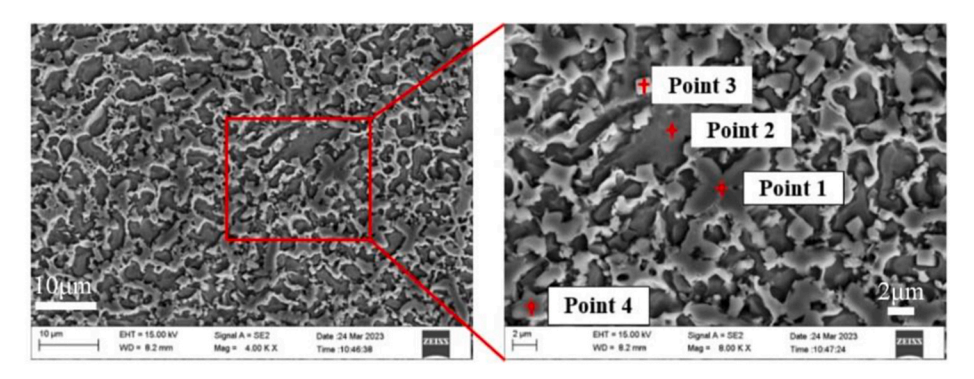


Fig. 9. The point scan results of sample S3.

melts, the free Ti and Cr atoms in the melting bath start to react with the C atoms in the graphite powder in an in-situ synthesis reaction to produce TiC and Cr carbides. However, Cr carbides are not stable at higher temperatures, so some of the precipitated Cr carbides will again react with the unreacted Ti atoms in an in-situ synthesis reaction. A relatively stable TiC phase is formed inside the nickel-based fusion cladding layer, which at the same time results in the segregation of the Cr element. In addition, the density of TiC particles is smaller than that of nickel-based alloys, so the TiC particles will migrate to the top of the melt pool. At the same time, the solid-liquid interface at the bottom of the molten pool has a small rate, which cannot catch up with the upward migration of TiC particles. Therefore, there are relatively few TiC particles at the bottom of the molten cladding layer, mostly in the middle and top regions of the molten cladding layer, which are usually distributed on the γ -Ni, Fe austenite dendrites or between the dendrites.

3.4. Microhardness analysis

The Vickers hardness at the cross-section of the cladding layer was measured by the indentation method. The results are shown in Fig. 12. It can be seen that from the top of the cladding layer to the substrate, the microhardness generally decreases. The microhardness of the workpiece can be divided into three parts, corresponding to the cladding layer, the bonding zone, and the substrate. The microhardness value at the substrate is about 285 HV $_{0.5}$. The microhardness of the bonding zone ranges from 300 HV $_{0.5}$ to 450 HV $_{0.5}$. The highest microhardness of the pure Ni45 cladding layer is 509.4 HV $_{0.5}$, while the highest microhardness in the area of the composite powder cladding layer is close to 850 HV $_{0.5}$. The microhardness values in the cladding layer of each workpiece are greater than those in the bonding zone. It is due to the dilution effect of

the substrate on the cladding layer, which results in the lower microhardness in the bonding zone. Moreover, Fig. 12 (a) also reveals that the microhardness value of the coating by the in situ synthesis method is excessively smooth. On the one hand, although the low density of TiC results in its upward flotation, the rapid solidification time of the melt pool is very short, often less than 1.0 s. In addition, the similar density of TiC and Ni-coated graphite induced a homogeneous distribution of solutes in the multiple liquid phases, and thus the TiC nucleation and growth are randomly located and homogeneous. On the other hand, the thermal conductivity of in situ synthesized TiC is much less than that of the metal matrix. Therefore, the orientation of the grains at the bottom of the molten pool is limited by the in-situ TiC, which decreases the anisotropy of each of the composite coatings and improves the smoothness of the mechanical properties [5,39]. From Fig. 12 (b), it can be seen that the average microhardness of the pure Ni45 cladding layer is 489.64 HV_{0.5}. The average microhardness of the cladding layer after the addition of different mass fractions of composite powder is 585.48 $HV_{0.5}$, 613.81 $HV_{0.5}$, 662.63 $HV_{0.5}$, and 753.83 $HV_{0.5}$, respectively. The average microhardness of the cladding layer after adding a reinforced phase is increased compared to the fused cladding layer without a reinforced phase. The average microhardness of the cladding layer is increased with the increase of the mass fraction of titanium powder and graphite. When the mass fraction of titanium powder and graphite powder reaches 20 %, the average microhardness of the cladding layer reaches 753.83HV_{0.5}, which is 2.65 times higher than that of the substrate, and 1.56 times higher than that of pure Ni45.

The microhardness of the cladding layer is mainly related to the size, content, morphology, and microstructure of the reinforcing phase particles in the coating. With the increase of (Ti $\,+$ C) mass fraction, the microhardness of the cladding layer gradually increases. The main

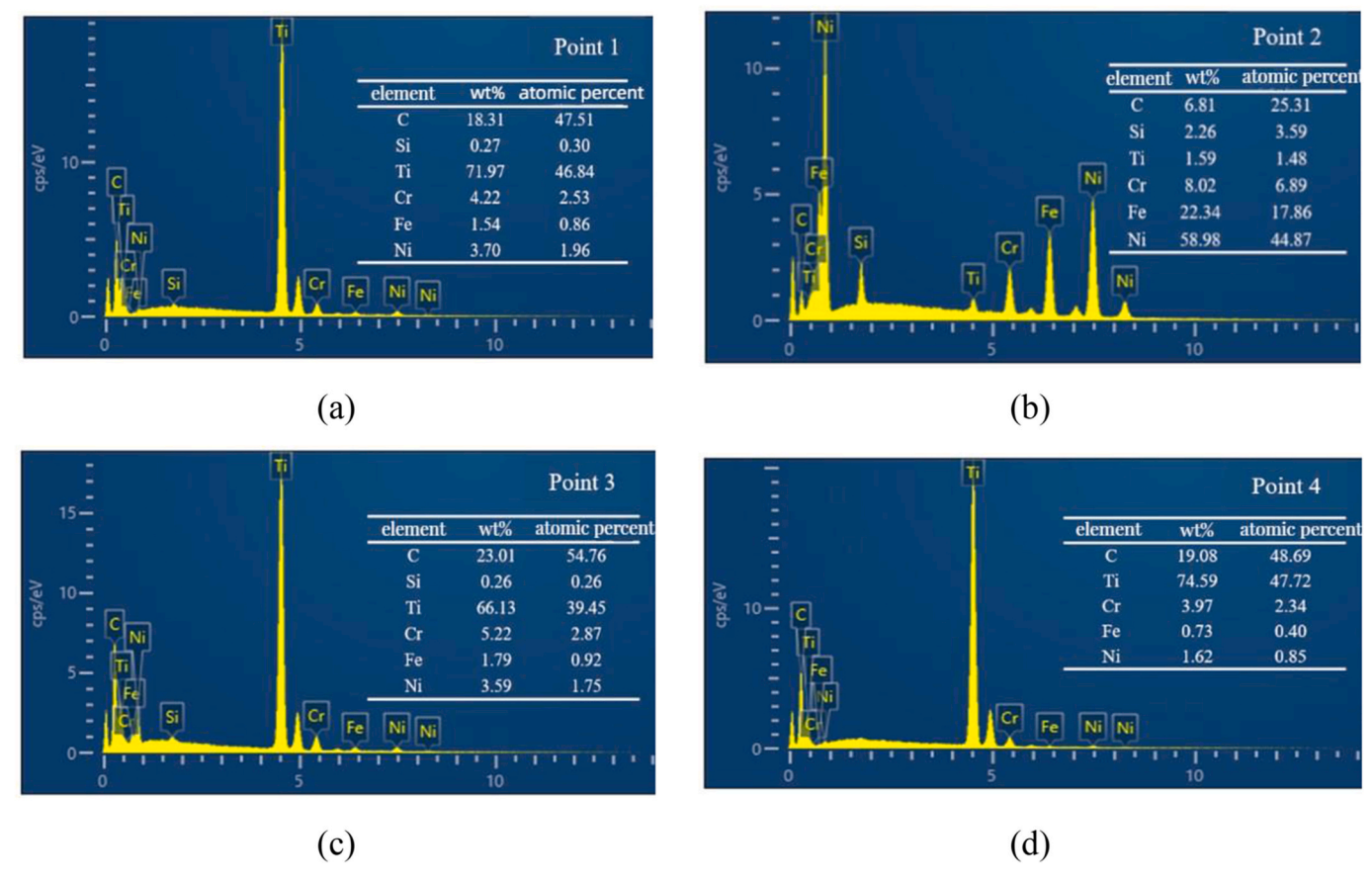


Fig. 10. The energy spectrum analysis of sample S3.

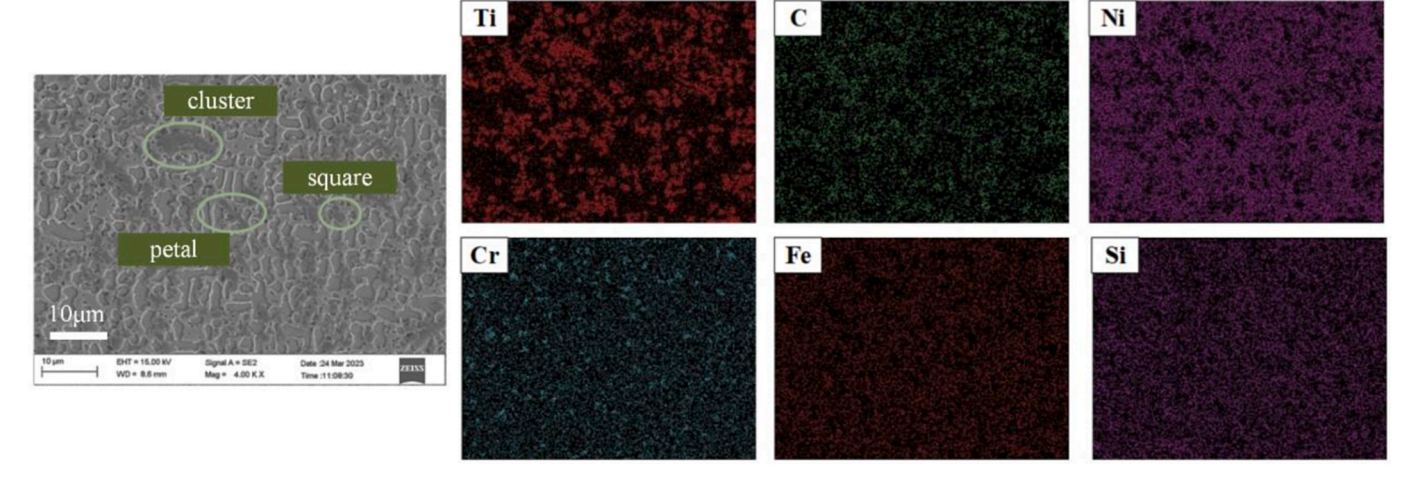


Fig. 11. The EDS surface scan results in the top zone of sample S4.

reason is that the C element in the nickel-coated graphite in-situ synthesizes TiC with the Ti element in the titanium powder, as well as with the Cr element to generate new phases such as other carbides with higher hardness. These compounds can effectively limit the dislocation movement and play the role of second-phase strengthening, thus improving the microhardness of the cladding layer.

3.5. Wear resistance analysis

The friction and wear performance of the cladding layer of each workpiece was tested, and the friction coefficient, wear volume, and

wear surface morphology were used as the main performance indexes to evaluate the wear resistance of TiC-reinforced composites [27,40]. As shown in Fig. 13, the comparisons of the friction coefficient of the substrate and the cladding layer with different contents of (Ti + C) show that the addition of (Ti + C)/Ni45 powder can effectively reduce the friction coefficient of the substrate and the Ni45 cladding layer. This is because the microhardness of the composite coatings increases gradually with the increase of the content of (Ti + C), which results in greater resistance to plastic deformation [8,41]. However, the average friction coefficient of the cladding layer increased rapidly when the added mass fraction was increased to 20 %. This is because the excessive mass

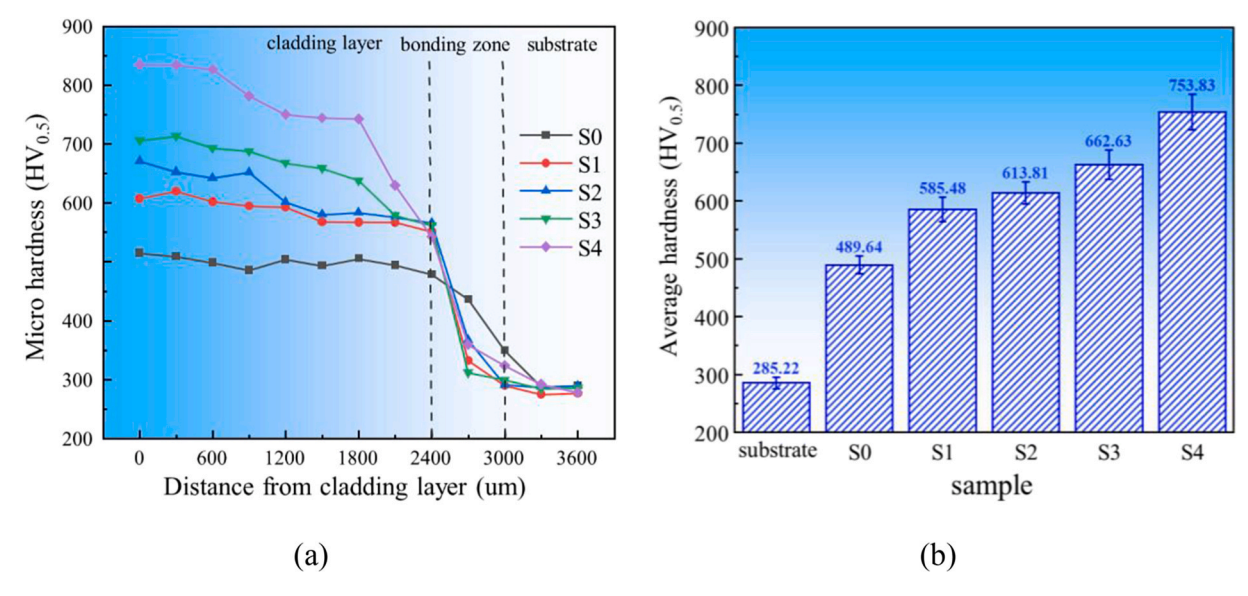


Fig. 12. The analysis results: (a) microhardness distribution; (b) average microhardness of each coating.

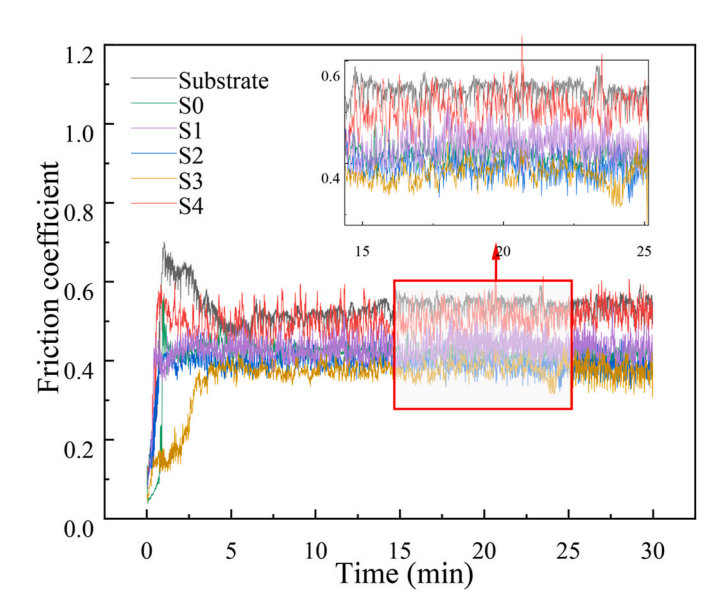


Fig. 13. Friction coefficient curve of each sample.

fraction of (Ti + C) in the workpiece S4 greatly increased the microhardness and generated excessive residual stress, which led to the emergence of more cracks and porosities, and these defects lowered the mechanical properties of the workpiece.

Combined with the three-dimensional morphology and two-dimensional profile of the wear tracks of each workpiece as shown in Figs. 14 and 15, it can be seen that the wear track depth of the substrate is the deepest, which is close to 8 μ m. The width of the wear track is also the largest, so the wear loss form is inferred as abrasive wear due to its low microhardness and good toughness [38,42]. With the addition of (Ti + C), the ability to withstand the deformation of the cladding layer is enhanced. The abrasion mark depth becomes shallower, and the width becomes smaller. When the mass fraction of (Ti + C) is 15 %, the depth of the wear track is the shallowest, about one quarter of the depth of the wear track of the substrate. When the (Ti + C) mass fraction was further increased, the defects such as porosity and cracks on the surface of the wear tracks became more and more numerous. While the width and depth of the wear tracks increased.

The volume loss results are shown in Fig. 14 (b). With the increase of

TiC content, the volume removal decreases from 1.55 to 0.34 $\rm mm^3$, which shows a 4.56 times increase in abrasion resistance compared to the substrate and exhibits better abrasion resistance. When the mass fraction of (Ti + C) reaches 20 %, the wear volume rises. This is due to the presence of more cracks and pores on the surface of workpiece S4, which reduces the performance of the cladding surface.

As shown in Fig. 16, the wear mechanism was further analyzed by combining the wear surface morphology of each workpiece. From Fig. 16 (a) and (a1), it can be seen that wear debris is attached to the substrate surface under the cyclic frictional shear action of the Al₂O₃ grinding head. Therefore, it can be judged that the form of wear is mainly adhesive wear. As shown in Fig. 16 (b) and (b1), the microhardness and strength of the cladding layer are enhanced after the addition of Ni45 powder. The wear debris generated under the damage of shear wear acts as abrasive particles in the subsequent wear process, which results in large material peeling, plowing, cracks, and other defects on the surface of the workpiece S0. Therefore there are adhesive wear and abrasive wear. The wear morphology of the cladding surface changes when different mass fractions of (Ti + C) are added. As the content increases, the large peeling phenomenon is gradually reduced. As shown in Fig. 16 (c) and (c1), When a 5 % mass fraction of (Ti + C)was added, the wear morphology was improved, but there were some protrusions resulting in an uneven surface. When the mass fraction of (Ti + C) was increased to 10 % as shown in Fig. 16 (d) and (d1), the peeling phenomenon was further reduced. When the (Ti + C) mass fraction is 15 % as shown in Fig. 16 (e) and (e1), the wear surface is improved significantly. Only a little peeling exists, and the surface is smooth and even. The coefficient of friction is the lowest, and the wear volume is also the smallest. At the same time, there are some pits on the surface of each workpiece, which are caused by the wear debris under the action of cyclic contact stresses. Thus it indicates the existence of fatigue wear and slight adhesive wear.

When the mass fraction of (Ti + C) is 20 % as shown in Fig. 16 (f) and (f1), it is obvious that the surface shows a lot of peeling again. The microhardness of the cladding layer is maximum, and the brittleness becomes larger. The toughness decreases, so the tendency of cracks in the cladding layer increases. Combined with the previous XRD analysis results, the peak of TiC is the strongest. The oxides generated by combining with oxygen elements increase during the wear process, such as TiO_2 . However, TiO_2 is brittle and prone to peeling under cyclic friction, which is also one of the reasons for the sudden increase in wear volume. The wear mechanism is dominated by oxidative and adhesive wear [29,34]. The peeling of the cladding layer makes the frictional

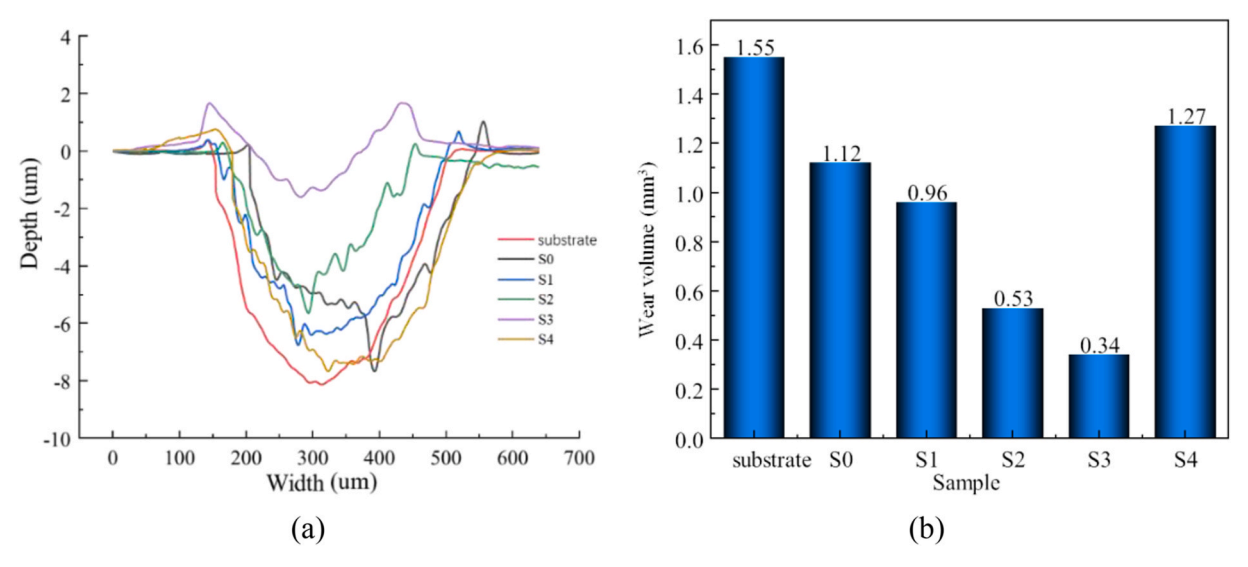


Fig. 14. The analysis results: (a) two-dimensional contour of wear mark; (b) the wear volume.

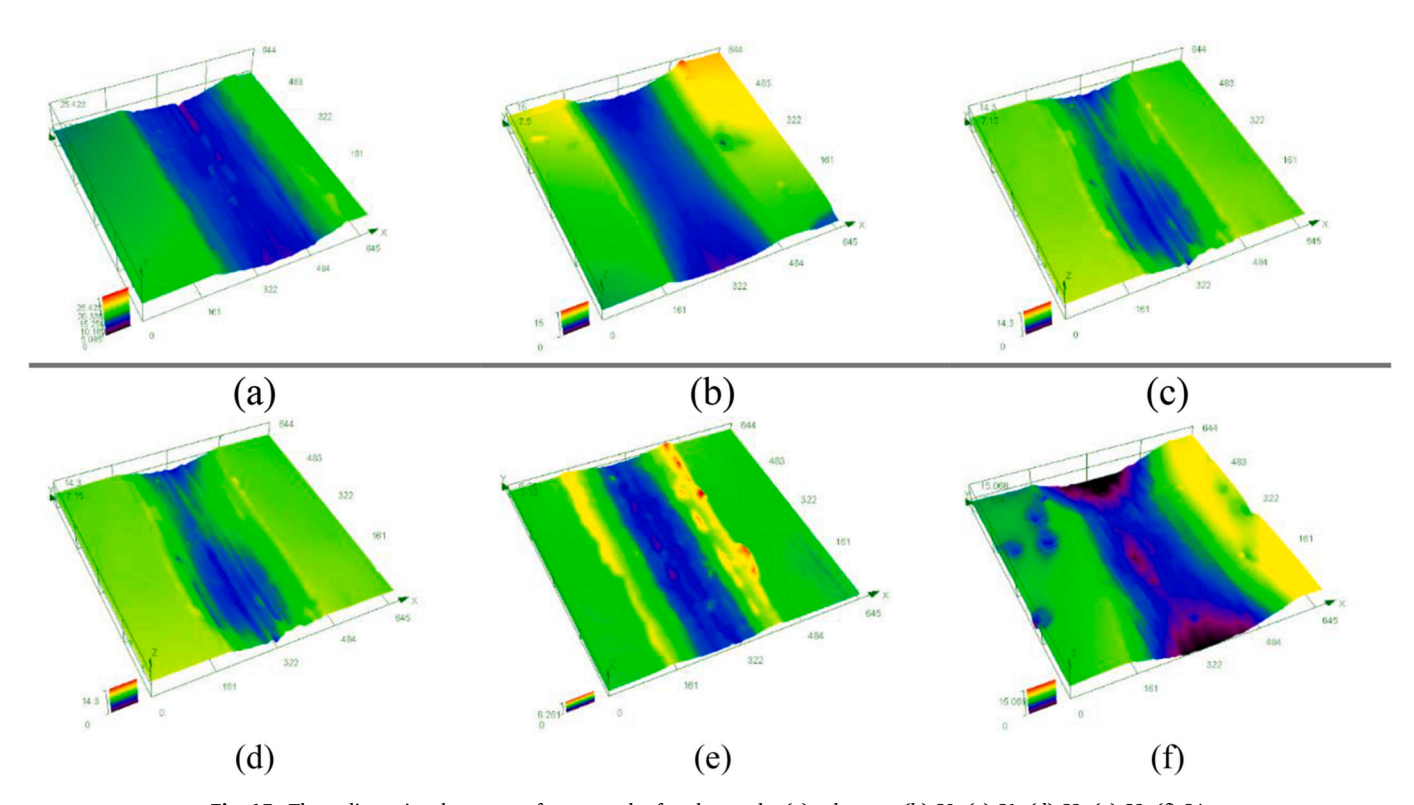


Fig. 15. Three-dimensional contour of wear track of each sample: (a) substrate; (b) S0; (c) S1; (d) S2; (e) S3; (f) S4.

resistance increase, resulting in a larger friction coefficient. The increased wear reduces the wear resistance of this workpiece to a certain extent.

As can be seen from the previous study, the wear morphology on the surface of workpiece S3 is better and has good wear resistance. Therefore, a further observation of the morphology by SEM is shown in Fig. 17. It can be seen that the wear surface of workpiece S3 has less wear debris, and the surface is relatively flat. There are also many TiC particles, and the generation of which improves the microhardness of the cladding layer [43,44]. The TiC particle takes the lead in contacting the abrasive ball in the wear experiment, which enhances the ability of the cladding surface to resist deformation.

The abrasion mark region was further analyzed by EDS surface

scanning, and the results are shown in Fig. 18. It can be seen that the Ti, C, and O elements are dominant, and the O element is uniformly distributed throughout the wear area. This proves the presence of an oxide film on the friction surface. It was deduced to be the oxide skin produced after the damage of the cladding layer surface during the wear experiment. It also proves that the wear mechanism is oxidative wear.

4. Conclusion

In this study, a series of TiC/Ni45 coatings were prepared by adding different Ti + C wt % particles to Ni45 powder using laser cladding technology. The effect of the content of in situ synthesized TiC on the physical phase, microstructure, microhardness, and wear resistance was

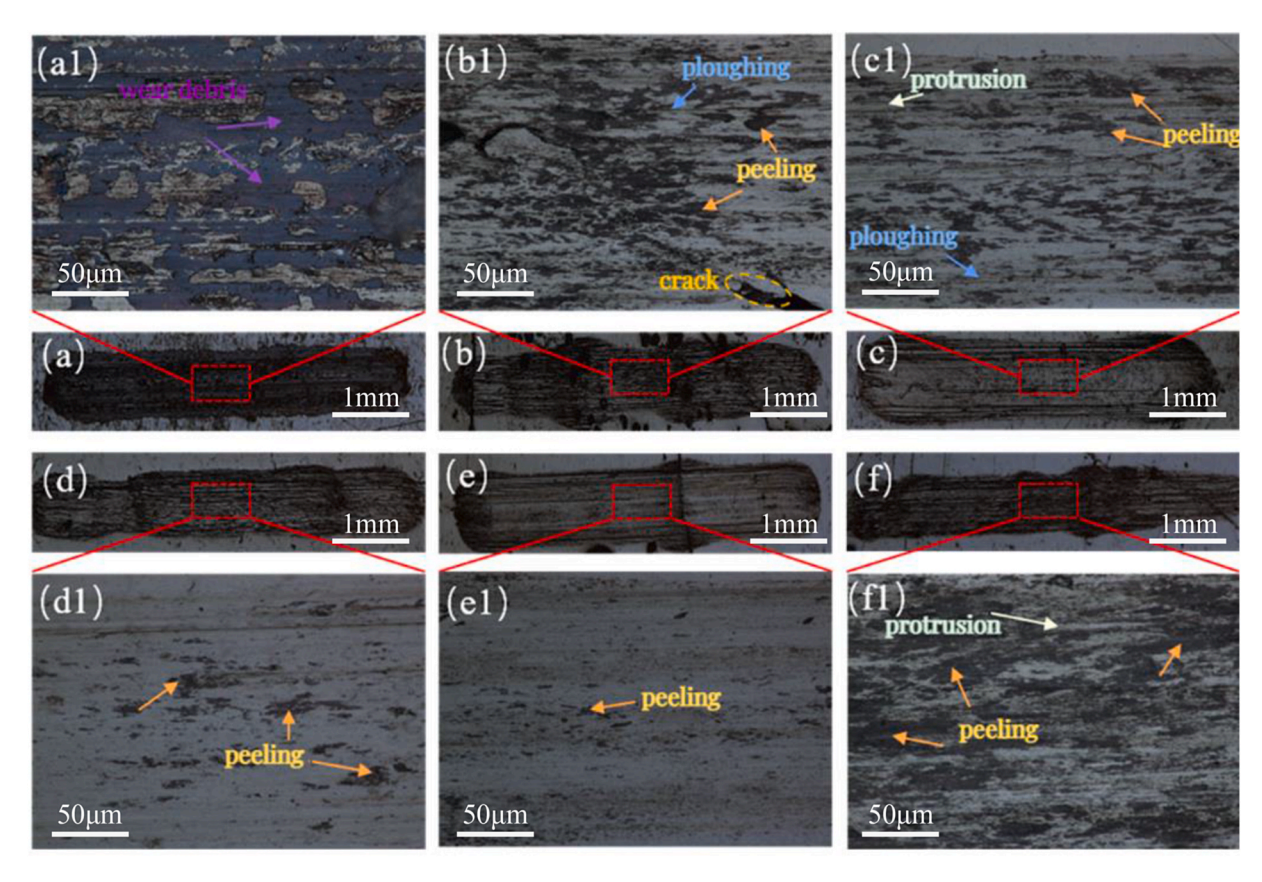


Fig. 16. The wear surface morphology: (a) substrate; (b) S0; (c) S1; (d) S2; (e) S3; (f) S4.

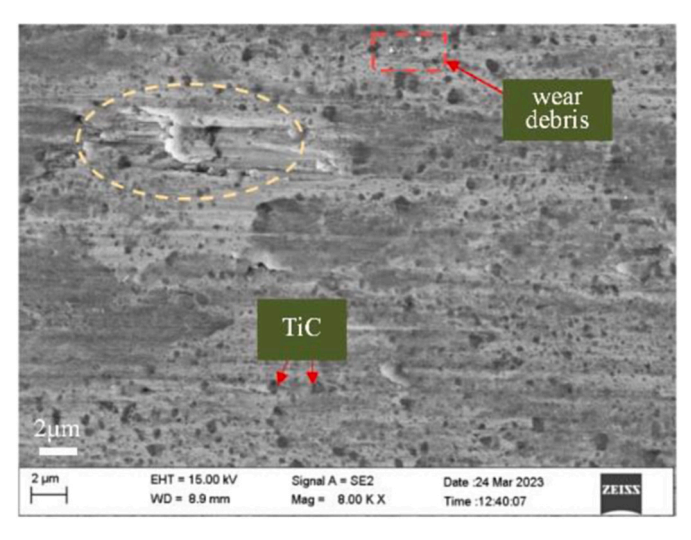


Fig. 17. The SEM image of the surface wear morphology of sample S3.

investigated and discussed in detail. The new findings and conclusions suggest that.

- (1) The physical phase composition of the Ni45 cladding layer is mainly γ -Ni phase, while with the addition of (Ti + C), the TiC phase began to appear. As the content of nickel-coated graphite and titanium powder increases, the peak of TiC is significantly enhanced, but no carbide phase of Cr is detected.
- (2) In the cladding layer, with the addition of (${\rm Ti}+{\rm C}$), the microstructure mainly consists of the white precipitation phase, black precipitation phase, and grey substrate. Combined with the EDS

- spectrometer analyses, it is inferred that the white precipitation phase is caused by the segregation of Cr elements, and the black precipitation phase is the TiC particles. With the increase of the mass fraction of (Ti + C), the TiC particles have different shapes, such as clusters, squares, and petals.
- (3) With the addition of (Ti + C), the microhardness of the cladding layer changed significantly. When the mass fraction of (Ti + C) reached 5 %, 10 %, 15 %, and 20 %, the average microhardness value of the cladding layer was improved to reach 585.48 HV_{0.5}, 613.81 HV_{0.5}, 662.63 HV_{0.5}, 753.83 HV_{0.5}, respectively. The average microhardness of the cladding layer with 20 wt% (Ti + C) is 2.65 times higher than that of the substrate and 1.56 times higher than that of the pure Ni45.
- (4) With the increase of (Ti+C) content, the average friction coefficient decreases gradually, and when the content reaches 15 %, the average friction coefficient reaches the minimum value. However, when the content of (Ti+C) continues to be added, the average friction coefficient suddenly becomes larger again.
- (5) With the increase of (Ti + C) content, the width and the depth of the abrasion mark decreases, and the wear volume is also gradually reduced. However, when the (Ti + C) mass fraction reaches 20 %, due to the increase in brittleness of the cladding layer, there are many surface defects and a large area of peeling phenomenon. It results in a larger abrasion mark width and poorer abrasion mark flatness. With the addition of (Ti + C), the wear mechanism is transformed from mainly adhesive wear to abrasive wear, oxidative wear, and fatigue wear.

CRediT authorship contribution statement

Juncai Li: Investigation. Yue Yang: Investigation, Resources. Liaoyuan Chen: Validation. Bojun Sun: Investigation. Zixuan Wang: Writing – original draft, Writing – review & editing. Tianbiao Yu:

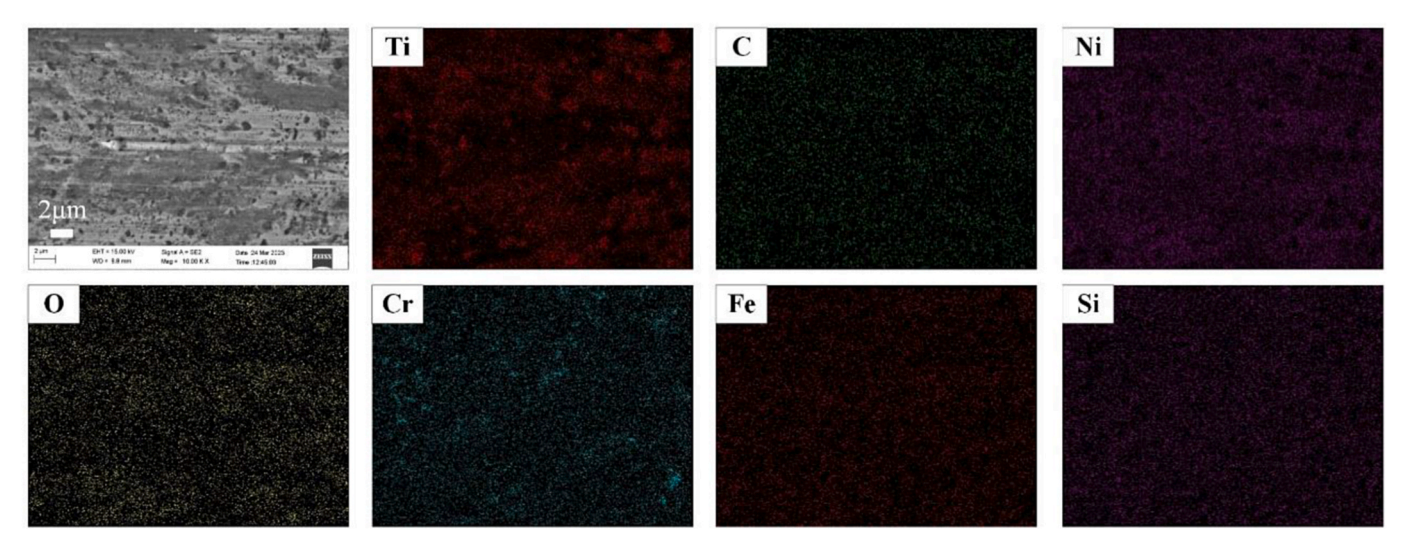


Fig. 18. The surface scan results of sample S3.

Supervision. Ji Zhao: Supervision.

Declaration of competing interest

The authors declare that they have no known competing financial interests or personal relationships that could have appeared to influence the work reported in this paper.

Acknowledgment

This work was supported by the National Natural Science Foundation of China (52075088, U23B20106), the China Postdoctoral Science Foundation (2021M700717), the Liaoning Provincial Natural Science Foundation of China (2023-MSBA-032), the Fundamental Research Funds for the Central Universities (N2203016, N2403018), the Northeastern University Postdoctoral Foundation (20210309), and the Fundamental Research Funds for the Education Department of Liaoning Province (LJKMZ20220348).

References

- H. Vasudev, G. Prashar, L. Thakur, A. Bansal, Electrochemical corrosion behavior and microstructural characterization of HVOF sprayed inconel-718 coating on gray cast iron, J. Fail. Anal. Prev. 21 (2021) 250–260, https://doi.org/10.1007/s11668-020-01057-8.
- [2] A. Bandyopadhyay, K.D. Traxel, M. Lang, M. Juhasz, N. Eliaz, S. Bose, Alloy design via additive manufacturing: advantages, challenges, applications and perspectives, Mater. Today 52 (2022) 207–224, https://doi.org/10.1016/j.mattod.2021.11.026.
- [3] J. Zhao, J. Ge, A. Khudoley, H. Chen, Numerical and experimental investigation on the material removal profile during polishing of inner surfaces using an abrasive rotating jet, Tribol. Int. 191 (2024) 109125, https://doi.org/10.1016/j. triboint.2023.109125.
- [4] G. Xiao, J. Wang, S. Zhu, Y. He, Z. Liu, Y. Huang, A review of research on material removal mechanisms for laser-assisted machining of difficult-to-machine materials, Surface Science and Technology 1 (2023), https://doi.org/10.1007/s44251-023-0007-4
- [5] L. Chen, Y. Chen, X. Chen, T. Yu, Z. Wang, Microstructure and properties of in situ TiC/Ni functionally gradient coatings by powder-fed laser cladding, Ceram. Int. (2022), https://doi.org/10.1016/j.ceramint.2022.08.243.
- [6] S. Saroj, C.K. Sahoo, M. Masanta, Microstructure and mechanical performance of TiC-Inconel 825 composite coating deposited on AISI 304 steel by TIG cladding process, J. Mater. Process. Technol. 249 (2017) 490–501, https://doi.org/ 10.1016/j.imatprotec.2017.06.042.
- [7] C. Xu, H. Zhang, S. Xiu, Y. Hong, C. Sun, Strengthening surface generation mechanism of carburization-assisted grinding, Surf. Technol. 52 (2023) 65–73, https://doi.org/10.16490/j.cnki.issn.1001-3660.2023.12.005.
- [8] F. Niu, W. Bi, C. Li, X. Sun, G. Ma, D. Wu, TiC ceramic coating reinforced 304 stainless steel components fabricated by WAAM-LC integrated hybrid manufacturing, Surf. Coating. Technol. 465 (2023) 129635, https://doi.org/ 10.1016/i.surfcoat.2023.129635.
- [9] L. Chen, T. Yu, X. Chen, Y. Zhao, C. Guan, Process optimization, microstructure and microhardness of coaxial laser cladding TiC reinforced Ni-based composite

- coatings, Opt Laser. Technol. 152 (2022) 108129, https://doi.org/10.1016/j.optlastec.2022.108129.
- [10] W. Li, C. Guo, S. Wu, M. Ying, W. Liu, Y. Li, G. Huang, T. Kang, Current research and development of arc additive manufacturing, J. Liaoning Inst. Technol. 30 (2023) 15–20. https://doi.org/10.3969/j.issn.1009-2269.2023.03.004.
- [11] C. Lu, B. Niu, K. Wang, J. Yi, G. Wang, H. Liang, X. Dong, Research status and development of arc additive manufacturing technology for mold repair, Metal Working (2024) 13–22, https://doi.org/10.3969/j.issn.1674-165X.2024.03.003.
- [12] L. Chen, Y. Zhao, X. Chen, T. Yu, P. Xu, Repair of spline shaft by laser cladding coarse TiC reinforced Ni-based coating: process, microstructure and properties, Ceram. Int. (2021), https://doi.org/10.1016/j.ceramint.2021.07.189.
- [13] X. Chen, Y. Liang, Z. Sun, Y. Zhao, Z. Ma, L. Chen, T. Yu, J. Zhao, Grinding performance oriented experimental evaluation on TiC-Steel cermet with vitrified bond cBN wheel, Ceram. Int. 47 (2021) 34949–34958, https://doi.org/10.1016/j. ceramit. 2021.09.036.
- [14] Y. Zhao, T. Yu, L. Chen, Y. Chen, C. Guan, J. Sun, Microstructure and wear resistance behavior of Ti–C–B4C-reinforced composite coating, Ceram. Int. 46 (2020) 25136–25148, https://doi.org/10.1016/j.ceramint.2020.06.300.
- [15] J. Luo, G. Zhu, J. Li, G. Xie, L. Wang, S. Shi, Numerical simulation on temperature field and flow field of molten pool in laser cladding, Surf. Technol. 52 (2023) 67–84, https://doi.org/10.16490/j.cnki.issn.1001-3660.2023.04.005.
- [16] A. Clare, O. Oyelola, J. Folkes, P. Farayibi, Laser cladding for railway repair and preventative maintenance, J. Laser Appl. 24 (2012) 32004, https://doi.org/ 10.2351/1.4710578.
- [17] S.R. Lewis, R. Lewis, D.I. Fletcher, Assessment of laser cladding as an option for repairing/enhancing rails, Wear 330–331 (2015) 581–591, https://doi.org/ 10.1016/j.wear.2015.02.027.
- [18] H. Guo, W. Wang, J. Guo, Q. Liu, Microstructure and wear performance of laser cladding Co-based alloy coatings of wheel/rail specimens, Mater. Sci. Technol. 23 (2015) 69–74.
- [19] H. Qi, Q. Xu, Y. Zhao, T. Guo, D. Ren, Study on realization method of automatic repair wear rail by laser cladding, J. Mech. Eng. 53 (2017) 160–165.
- [20] J. Yang, H. Liu, Research on the microstructure and properties of laser cladding Febase alloy on U71Mn rail surface, J. Rail. Eng. Soc. 7 (2010) 34–37.
- [21] J. Jiang, Y. Cheng, X. Huang, G. Lian, C. Chen, Performance of WC Reinforced Ni-Based Coating on 45 Steel Surface by Laser Cladding, Applied Laser 39 (2019) 24–34.
- [22] F. Li, X. Feng, Y. Chen, Influence of WC content on microstructure of WC/Ni60A laser cladding layer, Chin. J. Lasers 43 (2016) 403009.
- [23] L. Yang, Basic Research on Remanufacturing Process of Linear Guideway Based on Laser Cladding Technology, Northeastern University, 2018.
- [24] W. Cui, Y. Li, F. Li, X. Qi, X. Sun, Z. Pan, J. Niu, Wear and corrosion properties of in-situ TiC—TiB2 modified Ni-based composite coatings with different B/C ratios prepared by laser cladding, Ceram. Int. 50 (2024) 2424–2435, https://doi.org/ 10.1016/j.ceramint.2023.11.027.
- [25] D. Hu, Y. Liu, H. Chen, J. Liu, M. Wang, Effect of TiC addition on the microstructure and properties of Ni3Ta–TaC reinforced Ni-based wear-resistant coating, Ceram. Int. 47 (2021) 23194–23202, https://doi.org/10.1016/j. ceramint.2021.05.031.
- [26] S. Li, K. Huang, Z. Zhang, C. Zheng, M. Li, L. Wang, K. Wu, H. Tan, X. Yi, Wear mechanisms and micro-evaluation of WC + TiC particle-reinforced Ni-based composite coatings fabricated by laser cladding, Mater. Char. 197 (2023) 112699, https://doi.org/10.1016/j.matchar.2023.112699.
- [27] L. Chen, T. Yu, C. Guan, Y. Zhao, Microstructure and properties of metal parts remanufactured by laser cladding TiC and TiB2 reinforced Fe-based coatings, Ceram. Int. 48 (2022) 14127–14140, https://doi.org/10.1016/j. ceramint.2022.01.299.

- [28] Q. Mang, Y. Li, J. Wang, Effects of Ti addition on microstructure homogenization and wear resistance of wide-band laser clad Ni60/WC composite coatings, Int. J. Refract. Metals Hard Mater. 64 (2017) 225–233, https://doi.org/10.1016/j. iirmbm 2016 11 002
- [29] L. Chen, T. Yu, P. Xu, B. Zhang, In-situ NbC reinforced Fe-based coating by laser cladding: simulation and experiment, Surf. Coating. Technol. (2021) 127027, https://doi.org/10.1016/j.surfcoat.2021.127027.
- [30] D. Tijo, M. Masanta, A.K. Das, In-situ TiC-TiB2 coating on Ti-6Al-4V alloy by tungsten inert gas (TIG) cladding method: Part-I. Microstructure evolution, Surf. Coating. Technol. 344 (2018) 541–552, https://doi.org/10.1016/j. surfcoat.2018.03.082.
- [31] C. Guan, T. Yu, Y. Zhao, L. Chen, Y. Chen, Repair of gear by laser cladding Ni60 alloy powder: process, microstructure and mechanical performance, Appl. Sci. 13 (2023) 319, https://doi.org/10.3390/app13010319.
- [32] L. Chen, Y. Zhao, B. Song, T. Yu, Z. Liu, Modeling and simulation of 3D geometry prediction and dynamic solidification behavior of Fe-based coatings by laser cladding, Opt Laser. Technol. 139 (2021) 107009, https://doi.org/10.1016/j. optlastec.2021.107009.
- [33] K.D. Traxel, A. Bandyopadhyay, Modeling and experimental validation of additively manufactured tantalum-titanium bimetallic interfaces, Mater. Des. 207 (2021) 109793, https://doi.org/10.1016/j.matdes.2021.109793.
- [34] L. Chen, Y. Chen, X. Chen, T. Yu, Z. Wang, Microstructure and properties of in situ TiC/Ni functionally gradient coatings by powder-fed laser cladding, Ceram. Int. 48 (2022) 36789–36801, https://doi.org/10.1016/j.ceramint.2022.08.243.
- [35] D. Tijo, M. Masanta, In-situ TiC-TiB2 coating on Ti-6Al-4V alloy by tungsten inert gas (TIG) cladding method: Part-II. Mechanical performance, Surf. Coating. Technol. 344 (2018) 579–589, https://doi.org/10.1016/j.surfcoat.2018.03.083.
- [36] Y. Guo, C. Li, M. Zeng, J. Wang, P. Deng, Y. Wang, In-situ TiC reinforced CoCrCuFeNiSi0.2 high-entropy alloy coatings designed for enhanced wear

- performance by laser cladding, Mater. Chem. Phys. 242 (2020) 122522, https://doi.org/10.1016/j.matchemphys.2019.122522.
- [37] M. Ostolaza, J.I. Arrizubieta, A. Lamikiz, S. Plaza, N. Ortega, Latest developments to manufacture metal matrix composites and functionally graded materials through am: a state-of-the-art review, Materials 16 (2023) 1746, https://doi.org/10.3390/ ma16041746.
- [38] Y. Zhao, T. Yu, J. Sun, S. Jiang, Microstructure and properties of laser cladded B4C/TiC/Ni-based composite coating, Int. J. Refract. Metals Hard Mater. 86 (2020) 105112, https://doi.org/10.1016/j.ijrmhm.2019.105112.
- [39] K. Zhao, G. Zhang, G. Ma, C. Shen, D. Wu, Microstructure and mechanical properties of titanium alloy/zirconia functionally graded materials prepared by laser additive manufacturing, J. Manuf. Process. 56 (2020) 616–622, https://doi. org/10.1016/j.jmapro.2020.05.044.
- [40] W. Xi, B. Song, Z. Sun, T. Yu, J. Wang, Q. Sun, Effect of various morphology of in situ generated NbC particles on the wear resistance of Fe-based cladding, Ceram. Int. 49 (2023) 10265–10272, https://doi.org/10.1016/j.ceramint.2022.11.206.
- [41] A. Zabihi, R. Soltani, Tribological properties of B4C reinforced aluminum composite coating produced by TIG re-melting of flame sprayed Al-Mg-B4C powder, Surf. Coating. Technol. 349 (2018) 707–718, https://doi.org/10.1016/j. surfcoat.2018.06.040.
- [42] S. Sun, H. Fu, X. Ping, J. Lin, Y. Lei, W. Wu, J. Zhou, Reinforcing behavior and microstructure evolution of NbC in laser cladded Ni45 coating, Appl. Surf. Sci. 455 (2018) 160–170, https://doi.org/10.1016/j.apsusc.2018.05.199.
- [43] L. Yang, T. Yu, M. Li, Y. Zhao, J. Sun, Microstructure and wear resistance of in-situ synthesized Ti(C, N) ceramic reinforced Fe-based coating by laser cladding, Ceram. Int. 44 (2018) 22538–22548, https://doi.org/10.1016/j.ceramint.2018.09.025.
- [44] Q. Cheng, H. Chen, Y. Hou, Y. Xu, L. Fan, L. Dong, Microstructure and wear behavior of spherical NbC hardmetals with nickel-based binders on AISI 4145H steel, Int. J. Refract. Metals Hard Mater. 95 (2021) 105414, https://doi.org/ 10.1016/j.ijrmhm.2020.105414.